# Possible Bose-Einstein condensation of magnons in an $S=\frac{5}{2}$ honeycomb lattice

J. Khatua, <sup>1</sup> S. M. Kumawat, <sup>2</sup> G. Senthil Murugan, <sup>3</sup>, <sup>4</sup>, \* C.-L. Huang, <sup>2</sup> Heung-Sik Kim, <sup>5</sup>, <sup>6</sup> K. Sritharan, <sup>3</sup> R. Sankar,<sup>3,†</sup> and Kwang-Yong Choi <sup>1,‡</sup>

<sup>1</sup>Department of Physics, Sungkyunkwan University, Suwon 16419, Republic of Korea

<sup>2</sup>Department of Physics and Center for Quantum Frontiers of Research and Technology (QFort), National Cheng Kung University, Tainan, Taiwan

<sup>3</sup>Institute of Physics, Academia Sinica, Taipei 11529, Taiwan

<sup>4</sup>Department of Physics, St. Joseph's College of Engineering, OMR, Chennai 600 119, India

<sup>5</sup>Department of Semiconductor Physics and Institute of Quantum Convergence Technology, Kangwon National University, Chuncheon 24341, Republic of Korea

<sup>6</sup>Department of Energy Technology, Korea Institute of Energy Technology, Naju-si 58217, Republic of Korea



(Received 21 June 2025; revised 18 August 2025; accepted 30 September 2025; published 14 October 2025)

Quantum magnets offer a unique platform for exploring exotic quantum phases and quantum phase transitions through external magnetic fields. A prominent example is the field-induced Bose-Einstein condensation (BEC) of magnons near the saturation field. While this behavior has been observed in low-spin systems, its realization in high-spin, quasi-two-dimensional magnets-where multiple on-site excitations are possible-remains exceptionally rare. Here, we report thermodynamic and density functional theory results on single crystals of the honeycomb-lattice antiferromagnet  $K_4MnMo_4O_{15}$  with  $S=\frac{5}{2}$ . The system undergoes a field-induced transition to a fully polarized state at the critical field  $\mu_0 H_s = 6.4$  T. Our results reveal possible thermodynamic signatures of magnon BEC,  $T_N \sim (H_s - H)^{2/d}$  (d = 3), expanding the purview of BEC-driven quantum criticality to a high-spin, quasi-two-dimensional antiferromagnets with negligibly small anisotropy.

DOI: 10.1103/8wdy-2zbw

#### I. INTRODUCTION

Low-dimensional quantum magnets provide a fertile platform for realizing exotic quasiparticle excitations and exploring their many-body collective behavior [1–7]. External stimuli, particularly magnetic fields near the saturation point, can further induce novel quantum phases, resulting in rich phase diagrams with unconventional field-induced states including fractional magnetization plateaus [8,9], Bose-Einstein condensation (BEC) [2,10,11], spin-nematic [12–15], and supersolid phases [16,17].

Among quasiparticle excitations in magnetic systems, bosonic spin excitations such as magnon and triplon can, under suitable conditions, condense into a single quantum state—giving rise to the phenomenon known as BEC under magnetic fields [2,10]. This field-induced condensation represents a quantum phase transition and serves as a paradigmatic example of quantum criticality in some magnetic systems [11,18]. In earlier decades, aside from ultracold atomic gases, three-dimensional (3D) dimerized antiferromagnets—such as TlCuCl<sub>3</sub>, BaCuSi<sub>2</sub>O<sub>6</sub>, and Pb<sub>2</sub>V<sub>3</sub>O<sub>9</sub>—have been extensively studied as platforms for triplon BEC [11,19-22]. In these magnets an applied magnetic field closes the singlet-triplet gap, giving rise to field-induced XY-type magnetic order

\*Contact author: nanosen@gmail.com †Contact author: sankarndf@gmail.com ‡Contact author: choisky99@skku.edu

characterized by a low density of bosons [23]. However, in such 3D magnets, tuning the boson density via the Zeeman energy to approach the BEC quantum critical point (BEC-QCP) remains relatively unexplored due to the experimental challenges of reaching high magnetic fields required to overcome strong intradimer interactions [2,24,25].

In addition to BEC of triplons, conventional 3D and quasi-2D antiferromagnets exhibit field-induced saturation transitions, providing a versatile platform to study magnon BEC across a broad range of spin systems [26–29]. Within a widely discussed universal framework, the saturation field  $H_s$  marks the onset of magnon BEC, with the transition temperature scaling as  $T_N \propto (H_s - H)^{\alpha}$  with  $\alpha = 2/3$ , in agreement with mean-field predictions and independent of the spin quantum number [27,30,31]. While this universality is well established in many 3D spin systems, its validity in the quasi-2D limit is more subtle, with stability often strongly influenced by magnetic anisotropy.

Noticeably, magnon condensation in 2D ordered magnets initially received little attention in the context of BEC. Moreover, BEC in 2D systems was long considered unattainable due to the finite density of states at zero energy; instead, a Berezinskii-Kosterlitz-Thouless transition is typically expected near the saturation field [32–34]. However, recent observations of magnon BEC with an exponent  $\alpha = 1$ , in quasi-2D magnets with weak interplanar exchange interactions and easy-axis anisotropy have opened new avenues for exploring BEC-driven quantum criticality near the field-polarized phase, where 2D physics still dominates [35]. For example, the condensation of two-magnon bound state at the BEC-QCP driven by magnetic field and easy-axis anisotropy has been proposed in a nearly perfect S=1 triangular lattice Na<sub>2</sub>BaNi(PO<sub>4</sub>)<sub>2</sub> [36]. This system is particularly notable due to its weak exchange interactions, which allow the full temperature–magnetic field phase diagram to be mapped within a low field range of 2 T, revealing the elusive spin-nematic phase in proximity to the BEC-QCP [36]. Another example of magnon BEC in a quasi-2D honeycomb lattice is YbCl<sub>3</sub> ( $J_{\rm eff}=1/2$ ), which lies close to the 2D limit, with an interplanar-to-intraplanar coupling ratio of  $J_{\perp}/J=2\times 10^{-3}$  [35].

In large-spin systems (S>1), the presence of multiple internal spin levels on each site allows for a variety of excitation pathways, enabling richer collective behavior and potentially more complex forms of BEC [37]. A rare realization of a field-induced double BEC dome has been reported in the square-lattice compound  $\text{Ba}_2\text{Co}_{1-x}\text{Zn}_x\text{Ge}_2\text{O}_7$  ( $S=3/2;\ x=0.25$ ), where the first dome arises from condensation within the lowest spin doublet ( $|\pm\frac{1}{2}\rangle$ ), while the second emerges at higher magnetic fields, where a level crossing between the  $|+\frac{1}{2}\rangle$  and  $|+\frac{3}{2}\rangle$  states enables a secondary magnon condensation [38].

Motivated by the recent renewed interest in magnon BEC in 2D systems and the intriguing question of how dimensionality and magnetic anisotropy can critically shape the character of the BEC transition across a wide variety of spin systems, we explore the possibility of realizing BEC in single crystals of a honeycomb-lattice compound K<sub>4</sub>MnMo<sub>4</sub>O<sub>15</sub> (hereafter KMMO), where  $Mn^{2+}$  ions with spin S = 5/2form a 2D honeycomb network perpendicular to the crystallographic c axis. In zero field, KMMO undergoes long-range magnetic ordering at  $T_{\rm N}=2.21$  K, evidenced by a  $\lambda$ -like anomaly in the specific heat and in the temperature derivative of magnetic susceptibilities. Density functional theory (DFT) calculations reveal small intraplanar antiferromagnetic interactions of  $J_1 = 1.038$  K, along with much weaker interplanar and second-neighbor intraplanar couplings, consistent with a negative Curie–Weiss temperature. Upon applying a magnetic field perpendicular to the ab plane, the system evolves from Heisenberg-type order toward XY-like behavior, eventually entering a field-polarized phase beyond the critical field of  $\mu_0 H_s = 6.4$  T. At this transition, critical scaling of thermodynamic quantities provides signatures of the realization of a BEC-QCP in the 3D limit.

#### II. EXPERIMENTAL AND THEORETICAL DETAILS

Polycrystalline samples of KMMO have been prepared by the standard solid-state reaction method. High-purity starting materials of  $K_2CO_3$ , MnO, MoO<sub>3</sub> (with a purity of 99.95%) were thoroughly mixed and ground. The mixture was calcined in air at  $400\,^{\circ}\text{C}$  for 48 hours in a ceramic crucible. To achieve a single-phase compound, the sample was further sintered at 450 and  $500\,^{\circ}\text{C}$  for 48 hours, with intermediate grindings.

For single crystal growth, the polycrystalline powder was heated to  $550\,^{\circ}\text{C}$  at a rate of  $100\,^{\circ}\text{C/h}$ , held at  $550\,^{\circ}\text{C}$  for 48 hours, then cooled to 525 and  $500\,^{\circ}\text{C}$  at rate of  $0.5\,^{\circ}\text{C/h}$ , and finally cooled down to room temperature with a cooling rate

of 50 °C/h. Deep blue crystals ( $\sim$ 5 × 2 × 2 mm³) were successfully grown and mechanically collected from the crucible.

Powder x-ray diffraction (XRD) measurements were carried out at room temperature on crushed single crystals of KMMO using a Bruker AXS D8 Advance diffractometer with Cu K $\alpha$  radiation ( $\lambda = 1.54$  Å). The diffraction pattern was obtained with the x-ray beam aligned perpendicular to the (h00) planes of a single crystal using the same setup.

Magnetic measurements were carried out using a superconducting quantum interference device vibrating-sample magnetometer (SQUID-VSM, Quantum Design, USA) in the temperature range 2 K  $\leqslant$  T  $\leqslant$  300 K and in magnetic fields up to 7 T. Additional magnetization measurements were performed using the  $^3\text{He}$  option of the MPMS3 SQUID magnetometer from Quantum Design. Specific heat measurements were conducted using a standard relaxation method with a physical property measurement system (PPMS, Quantum Design, USA) in the temperature range 0.13 K  $\leqslant$  T  $\leqslant$  300 K in several magnetic fields up to 9 T.

DFT calculations were carried out using the OpenMX code with the Perdew–Burke–Ernzerhof (PBE) generalized gradient approximation (GGA) as the exchange-correlation functional [39]. To account for strong electronic correlations in Mn atoms, a Hubbard on-site Coulomb parameter U was applied with varying values. The plane-wave energy cutoff was set to 300 Ry, and self-consistent field (SCF) convergence was achieved with a threshold of  $1.0 \times 10^{-9}$  Hartree. The Brillouin zone was sampled using a  $4 \times 4 \times 6$  Monkhorst–Pack k-point mesh. SCF iterations employed the RMM-DIIS mixing scheme, with a maximum of 300 steps and adaptive mixing parameters.

The converged SCF results from OpenMX served as input for the  $J_X$  code [40], which evaluates exchange coupling parameters  $J_{ij}^{\text{GGA}}$  between localized spins based on the Green's function formulation of the Liechtenstein approach.

## III. RESULTS AND DISCUSSION

#### A. Crystal structure

To confirm the crystal structure of KMMO, Rietveld refinement of powder XRD data-obtained from crushed single crystals-was carried out at room temperature. The refinement results indicate that the title compound KMMO crystallizes in a trigonal structure (space group P -3) with the lattice parameters a = b = 10.37 Å, c = 8.16 Å, and angles  $\alpha = \beta = 90^{\circ}$ ,  $\gamma = 120^{\circ}$ . The obtained lattice parameters and atomic coordinates (not shown here) are consistent with earlier reported values [41]. Figure 1(a) shows a schematic of several unit cells of KMMO, where the magnetic Mn<sup>2+</sup> ions occupy a unique crystallographic site, without any detectable antisite disorder among the constituent ions. Interestingly, the Mn<sup>2+</sup> ions form a nearly perfect 2D honeycomb lattice with a nearest-neighbor distance of 6.01 Å, oriented perpendicular to the c axis. Notably, the interplanar Mn–Mn distance (8.16 Å) is shorter than the intraplanar second-nearest-neighbor distance (10.37 Å). Each Mn<sup>2+</sup> ion is coordinated by six O<sup>2-</sup> ions, forming an MnO<sub>6</sub> octahedron. Two of these oxygen atoms are shared with the two adjacent MoO<sub>4</sub> tetrahedra, each of which shares one of its corners with the nearest-neighbor oxygen atoms of

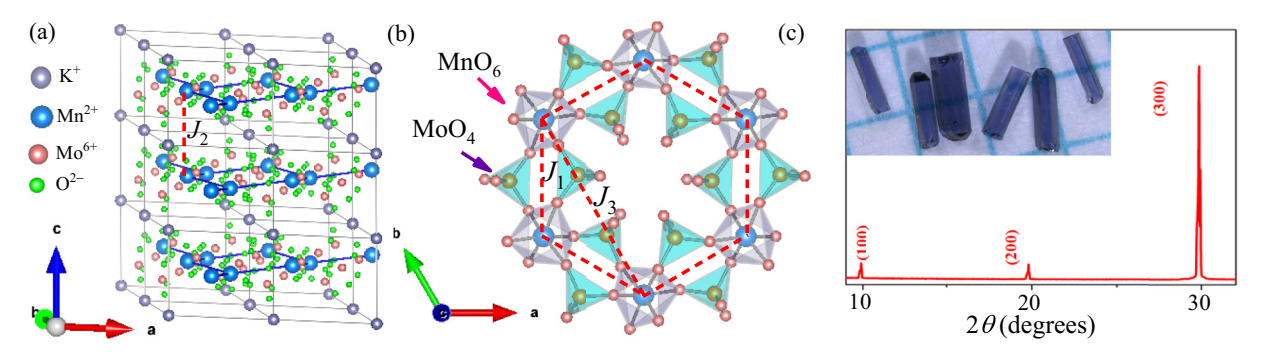


FIG. 1. (a) Schematic of unit cells of  $K_4MnMo_4O_{15}$ , where  $Mn^{2+}$  ions form a honeycomb lattice stacked along the c axis. The interplanar interaction is indicated by the red dotted line labeled as J2. (b) Perpendicular view of the honeycomb plane formed by octahedrally coordinated  $Mn^{2+}$  ions, where each  $Mn^{2+}$  ion is connected to its nearest neighbor via the  $Mn^{2+}$  interactions are labeled as  $J_1$  and  $J_3$ , respectively. (c) Powder x-ray diffraction pattern of a single crystal which has a preferred orientation of indexed (h00) peaks. Inset shows the optical images of single crystals of  $K_4MnMo_4O_{15}$ .

the  $MnO_6$  octahedron [see Fig. 1(b)]. This arrangement establishes an intraplanar nearest-neighbor superexchange pathway mediated through the Mn-O-Mo-O-Mn connection. The XRD pattern obtained with the incident beam oriented perpendicular to the (h00) plane is shown in Fig. 1(c), which corresponds to the orientation perpendicular to the honeycomb plane. The inset of Fig. 1(c) displays photos of KMMO crystals with their top surfaces corresponding to the (h00) plane.

#### B. Thermodynamic properties and DFT calculations

In order to investigate the behavior of local moments of Mn<sup>2+</sup> (S = 5/2) ions, their exchange interactions, and anisotropic properties, magnetic susceptibility ( $[\chi(T)]$  measurements were performed in a field of  $\mu_0 H = 0.01$  T applied parallel and perpendicular to the ab plane as shown in Fig. 2(a). Upon lowering the sample temperature,  $\chi(T)$  exhibits no significant directional dependence at high temperatures; however, deviations between the two directions begin to emerge below 30 K, indicating the onset of magnetic correlations with moderate anisotropy. Above T > 30 K, the inverse susceptibility remains linear, indicating the Curie-Weiss (CW) regime, and is well described by the CW law,  $\chi(T) = \chi_0 + C/(T - \theta_{\text{CW}})$ . Here,  $\chi_0$  represents the temperature-independent contributions from core diamagnetism and Van Vleck paramagnetism, C is the Curie constant, and  $\theta_{CW}$  reflects the strength and nature of magnetic exchange interactions. The green solid line in Fig. 2(a) represents the CW fit, yielding  $\chi_0 = -3.27 \times$  $10^{-4}$  cm<sup>3</sup>/mol,  $C = 4.7 \pm 0.01$  cm<sup>3</sup>K/mol, and  $\theta_{CW} =$  $-9 \pm 0.25$  K. The calculated effective magnetic moment  $\mu_{\rm eff} = \sqrt{8C} = 6.13 \,\mu_{\rm B}$  is slightly larger than the spin-only value of  $\mu_{\rm eff} = 5.91 \ \mu_{\rm B}$  for high-spin Mn<sup>2+</sup>( $S = \frac{5}{2}$ ) [42]. The obtained negative CW temperature indicates that the dominant magnetic interactions between the  $S = \frac{5}{2}$  moments are antiferromagnetic in nature.

Upon further cooling below 30 K,  $\chi(T)$  increases monotonically for both directions ( $\chi_{\perp}$  and  $\chi_{\parallel}$ ), reaching a broad maximum around  $T_{\rm max}=4.2$  K, indicating the presence of short-range spin correlations (SRO), typical of low-dimensional magnetic systems [25]. Below  $T_{\rm max}$ ,  $\chi_{\perp}$  begins to decrease, with a distinct change in slope across  $T_{\rm N}=2.21$  K,

as evidenced by the anomaly in  $d\chi(T)/dT$  shown in the inset of Fig. 2(a). In contrast,  $\chi_{\parallel}$  continues to increase, displaying a weak dip near  $T_{\rm N}$ . The observation of  $\chi_{\parallel} > \chi_{\perp}$  suggests the presence of easy-plane anisotropy. Figure 2(b) shows the isothermal magnetization as a function of magnetic field, which tends toward saturation above 7 T, consistent with the estimated CW temperature. It is worth noting that the

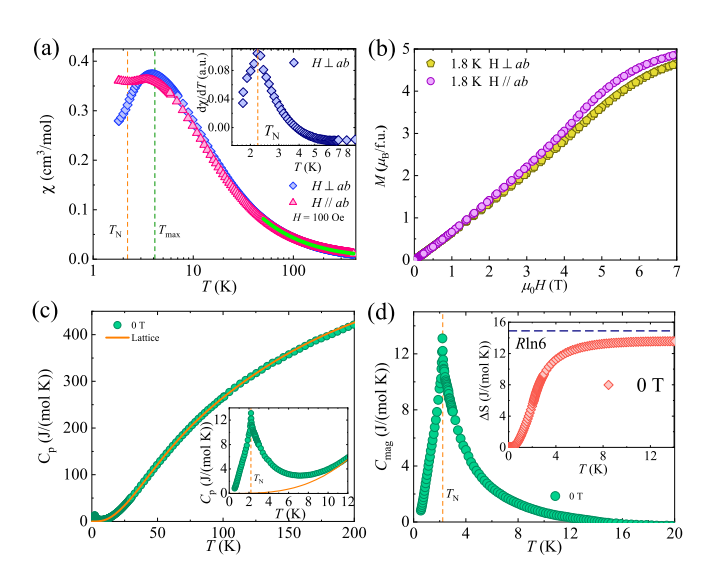


FIG. 2. (a) Temperature dependence of magnetic susceptibility measured in a field of  $\mu_0 H = 0.01$  T applied parallel and perpendicular to the ab plane, with the x axis plotted on a logarithmic scale. The solid green line represents the Curie-Weiss fit, while the dashed vertical lines indicate the broad maximum at  $T_{\text{max}} = 4.2 \text{ K}$ and the Néel temperature at  $T_{\rm N} = 2.21$  K. The top inset displays the derivative of magnetic susceptibility as a function of temperature for the field applied perpendicular to the ab plane. (b) Isothermal magnetization as a function of magnetic field parallel and perpendicular to the ab plane at 1.8 K. (c) Temperature dependence of specific heat in zero field, where the solid orange line represents the Debye-Einstein model of the lattice contribution. The bottom inset enlarges the low-temperature region, revealing an anomaly at  $T_{\rm N}$ . (d) Magnetic specific heat as a function of temperature showing an anomaly at  $T_N$ . The top inset shows the temperature dependence of the calculated entropy change in zero field.

isothermal magnetization exhibits no noticeable anisotropy up to 1.6 T, beyond which a moderate anisotropic behavior begins to emerge. This crossover may be associated with the transition from Heisenberg-like to *XY*-like antiferromagnetic behavior, as also supported by the field-dependent specific heat measurements (see below).

To further confirm the presence of long-range magnetic order, specific heat  $(C_p)$  measurements were performed in zero field as shown in Fig. 2(c).

A clear  $\lambda$ -like anomaly is observed around  $T_N$  [see inset of Fig. 2(c)] which corresponds to the anomaly observed in the  $d\chi/dT$  data, further supporting the presence of long-range magnetic order in KMMO. To subtract the phonon contribution to the specific heat, the  $C_p$  data were fitted [solid orange line in Fig. 2(c)] using a model comprising one Debye term and three Einstein terms, i.e.,  $C_{\text{latt}}(T) = C_D[9R(\frac{T}{\theta_D})^3 \int_0^{\theta_D/T} \frac{x^4 e^x}{(e^x - 1)^2} dx] +$  $\sum_{i=1}^{3} C_{E_i} [R(\frac{\theta_{E_i}}{T})^2 \frac{e^{\theta_{E_i}/T}}{(e^{\theta_{E_i}/T} - 1)^2}], \text{ where } \theta_D = 120 \pm 0.30 \text{ K is}$ the Debye temperature,  $\theta_{E_1} = 177 \pm 0.54$  K,  $\theta_{E_2} = 302 \pm$ 0.76 K, and  $\theta_{E_3} = 671 \pm 1.6$  K are the Einstein temperatures of the three optical phonon modes, and R is the molar gas. To reduce the number of fitting parameters,  $C_D$  was fixed at 3 to represent the three acoustic phonon modes, while  $C_{E_1} = 15$ ,  $C_{E_2} = 20$ , and  $C_{E_3} = 25$  were assigned to account for the 69 optical modes, corresponding to the (3n-3) optical branches for n = 24 atoms in KMMO [43]. After subtraction of the lattice contributions, the resulting magnetic specific heat is shown in Fig. 2(d), revealing an anomaly around  $T_N$ and indicating that magnetic correlations begin to develop at temperatures higher than the CW temperature, consistent with the  $\chi(T)$  data. Next, the change of magnetic entropy associated to the magnetic ordering was calculated by integrating the magnetic specific heat divided by temperature as shown in the inset of Fig. 2(d). The total entropy released above the CW temperature is about 13.65 J/mol·K, corresponding to roughly 91% of the expected value,  $R \ln(2S + 1)$ , for a S = 5/2 system. The missing 10% of the entropy might be due to the overestimation of lattice contribution or because of short-range spin correlations that exist above  $T_N$ . Interestingly, only about 40% of the total entropy is released at  $T_N$ , meaning that the rest is released at higher temperatures due to shortrange magnetic interactions. This agrees well with the broad maximum seen in the temperature dependence of the  $\chi(T)$ data [Fig. 2(a)].

In order to determine a spin Hamiltonian of KMMO, we computed the interatomic exchange interactions using the magnetic force linear response theory [44]. This approach allowed us to quantify the strength of intraplanar nearestneighbor  $(J_1)$  and second-nearest-neighbor  $(J_3)$  interactions, as well as the interplanar coupling  $(J_2)$  [see Figs. 1(a) and 1(b)]. Figure 3 presents the variation of these three exchange interactions as a function of the on-site Coulomb interaction U. It reveals the presence of a dominant antiferromagnetic nearest-neighbor exchange interaction  $J_1$  while  $J_2$  and  $J_3$  remain relatively weak. Using the calculated  $J_1 = 1.038$  K,  $J_2 = -0.073$  K, and  $J_3 = 0.0165$  K for U = 7 eV, the Curie–Weiss temperature was estimated using the relation  $\theta_{\rm CW} = S(S+1)(3J_1+2J_2+6J_3)/3$ , yielding  $|\theta_{\rm CW}| \approx 9.03$  K, in good agreement with the experimental

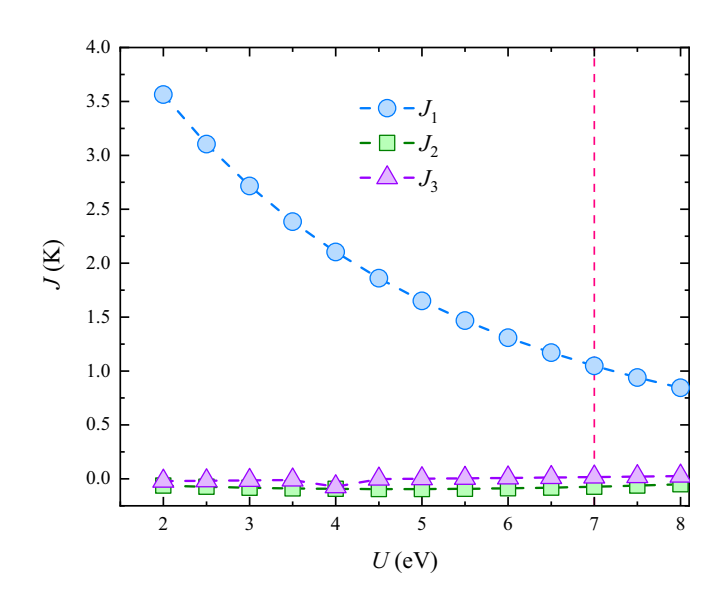


FIG. 3. Variation of the three exchange interactions with respect to the on-site Coulomb interaction strength U. The vertical dashed pink line indicates the specific value for which the calculated exchange couplings reproduce the experimental Curie–Weiss temperature.

value. The weak second-neighbor exchange within the honeycomb plane underscores that the origin of  $T_{\rm N}$  being well below  $\theta_{\rm CW}$  is due to the low-dimensional nature of the system, while long-range magnetic order likely arises from a combination of interplanar coupling and weak easy-plane anisotropy.

#### C. Field-induced thermodynamic properties

To further explore the field-tunable magnetic ground state, thermodynamic measurements were carried out at several fields applied perpendicular to the ab plane. Figure 4(a)presents the isothermal magnetization at several temperatures, while its field derivative is plotted in Fig. 4(b). In the antiferromagnetic state below  $T_N$ , magnetization responds linearly to the applied field up to 4 T. A steeper rise at higher fields reflects a transition toward the fully polarized (FP) phase. The critical field  $(\mu_0 H_s)$  associated with this field-induced transition is identified by an anomaly in the field derivative of the magnetization [see Fig. 4(b)]. The dashed vertical line at  $\mu_0 H_s = 6.4$  T indicates the quantum critical point at the saturation field for the titled compound KMMO, as determined from field-dependent specific heat measurements at T = 0.3 K (see below). As the temperature approaches  $T_{\rm N}$ , the field-induced anomaly in dM/dH [Fig. 4(b)] gradually disappears due to enhanced thermal fluctuations.

Figure 4(c) shows the temperature dependence of  $\chi(T)$  under several magnetic fields at low temperatures. The dashed vertical lines correspond to  $T_{\rm max}=4.2$  K, associated with SRO, and the Néel temperature  $T_{\rm N}$ , determined from the anomaly in  $d\chi/dT$  [see Fig. 2(b)] at  $\mu_0H=0.01$  T. As the magnetic field increases,  $T_{\rm max}$  shifts to lower temperatures (orange arrow), while  $T_{\rm N}$  initially shifts to higher temperatures (star pink arrow) before decreasing at higher fields. This nonmonotonic behavior of  $T_{\rm N}$  suggests a crossover from Heisenberg to XY-type spin order under an applied magnetic

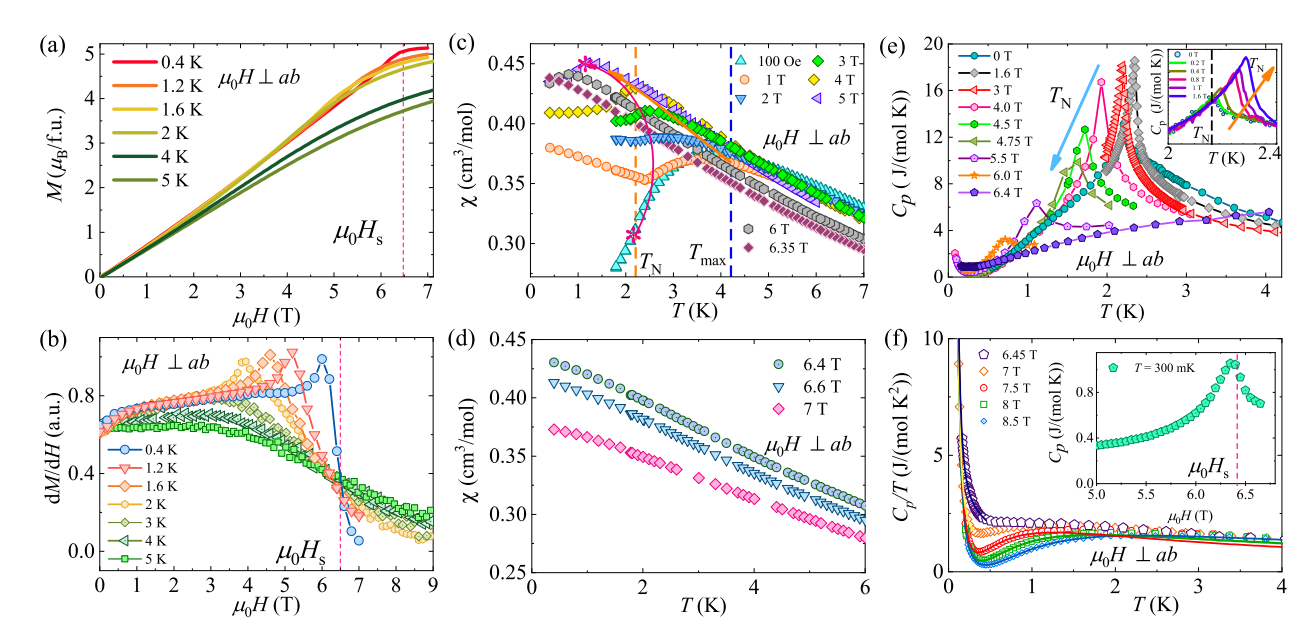


FIG. 4. (a) Isothermal magnetization as a function of magnetic field and (b) its derivative. The dashed vertical lines indicate the position of the quantum critical point at the saturation field  $\mu_0 H_s = 6.4$  T. (c) Temperature dependence of magnetic susceptibility at low temperatures under several magnetic fields. Dashed vertical lines indicate  $T_N$  and  $T_{max}$  at  $\mu_0 H = 0.01$  T, with their field-dependent shifts highlighted by orange arrows (for  $T_{max}$ ) and pink star arrows (for  $T_N$ ). (d) Temperature dependence of magnetic susceptibility in fields  $\mu_0 H \ge 6.4$  T at low temperatures. (e) Temperature dependence of specific heat at low-temperatures in several fields. The inset shows a magnified view of the anomaly up to 1.6 T. The orange and sky-blue arrows indicate the progressive shifts of  $T_N$  toward higher and lower temperatures, respectively. (f) Temperature dependence of specific heat divided by temperature for fields  $\mu_0 H > 6.4$  T. The solid lines represent a combination of fits to the nuclear Schottky contribution and the gapped behavior, as described in the text. Inset shows the field-dependent specific heat at T = 300 mK. In all panels, the magnetic field was applied perpendicular to the ab plane.

field, which arises from the interplay between spin dimensionality, anisotropy, and Zeeman energy in near-isotropic Heisenberg magnets with small single-ion anisotropy. More specific, when a magnetic field is applied perpendicular to the easy plane, the magnetic field quenches the out-of-plane spin fluctuations, effectively leading to a dimensional reduction in spin space [35]. For fields  $\mu_0 H_s \ge 6.4$  T,  $\chi(T)$  [Fig. 4(d)] exhibits a monotonic increase with decreasing temperature, along with progressively reduced  $\chi(T)$  values with increasing field, consistent with a FP phase. In this regime, the external field aligns the magnetic moments, suppressing thermal spin fluctuations and reducing the system's susceptibility to respond to further changes in field, resulting in lower  $\chi(T)$ .

To support the symmetry crossover observed in the  $\chi(T)$ data and to accurately determine the critical field, specific heat serves as a powerful probe. Figure 4(e) presents the temperature dependence of  $C_p$  under several magnetic fields. With increasing field, the  $\lambda$ -like anomaly becomes more pronounced and shifts to higher temperatures up to 1.6 T [as indicated by the orange arrow in the inset of Fig. 4(e)]. Beyond this field, the anomaly gradually moves to lower temperatures, consistent with a crossover from Heisenberg to XY-type spin order, as also reflected in the  $\chi(T)$  data. Interestingly, the  $\lambda$ -like anomaly is completely suppressed at the critical field  $\mu_0 H_s = 6.4$  T. Below 0.5 K, the upturn in the specific heat is attributed to nuclear Schottky contributions, exhibiting the characteristic  $1/T^2$  dependence [35]. The presence of the critical field is further supported by an anomaly observed in the field-dependent  $C_p$  data at 0.3 K, as shown in the inset of Fig. 4(f).

To investigate the FP phase,  $C_p$  measurements were carried out at several fields above  $\mu_0 H_{\rm s}$ . Figure 4(f) presents  $C_p/T$  as a function of temperature, revealing a broad maximum at higher temperatures and a pronounced upturn at low temperatures, indicating the presence of a field-induced gap and nuclear Schottky contribution, respectively. The solid line in Fig. 4(f) represents a fit using the model  $C_p(T) \propto 1/T^2 + \exp(-\Delta/T)$  [35], where  $\Delta$  represents the value of field-induced gap. The obtained gap values are plotted in orange squares of Fig. 5(a).

#### D. Magnetic phase diagram and critical scaling behavior

To provide a comprehensive picture of the evolution of the field-induced phase transition from the antiferromagnetic (AFM) to the FP phase, we constructed the temperature—magnetic field phase diagram [Fig. 5(a)] based on the thermodynamic results. The different regions are labeled according to the interpretations discussed in Secs. III B and III C. Above  $\mu_0 H_s$ , a gapped FP phase emerges. With increasing magnetic field, the estimated gap value follows a linear dependence of the form  $g\mu_B(H-H_s)$  [Fig. 5(a)], yielding g=1.66. This effective g value is somewhat lower than the typical g factor  $g \sim 2.0$  for Mn<sup>2+</sup> ions. The phase boundaries are plotted over the contour map of the magnetic specific heat divided by temperature.

To assess whether the field-induced phase transition near  $\mu_0 H_s$  can be characterized as a BEC-QCP of magnons, we plotted  $T_{\rm N}$  as a function of  $\mu_0 (H_s - H)$  [2]. Remarkably, the data follow a power-law behavior  $T_{\rm N} \propto (H_s - H)^{0.60 \pm 0.01}$ 

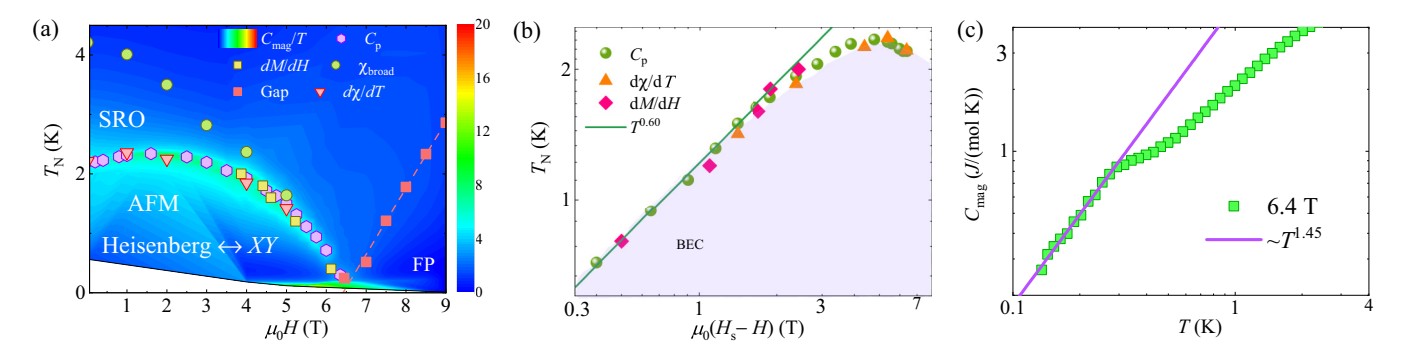


FIG. 5. (a) Temperature–magnetic field phase diagram with phase boundaries determined from the thermodynamic measurements, as indicated in the legend. The background shows a contour map of the magnetic specific heat divided by temperature. The dashed red line shows a linear field dependence of gap. (b) Scaling behavior of  $T_N$  as a function of  $\mu_0(H_s-H)$  on a logarithmic scale. (c) Temperature dependence of magnetic specific heat at the critical field  $\mu_0H_s=6.4$  T on a logarithmic scale. The solid line indicates a  $\sim T^{1.45}$  power-law behavior.

[Fig. 5(b)], consistent with the BEC universality class in 3D XY-type antiferromagnets, where  $T_{\rm N} \sim (H_{\rm s}-H)^{2/d}$  (d=3) is expected [2,35]. Additionally, the magnetic specific heat after subtracting the nuclear Schottky contribution exhibits a power-law dependence  $C_{\rm mag} \propto T^{1.45\pm0.02}$ , aligning with the  $T^{d/2}$  behavior predicted for BEC in 3 D systems [Fig. 5(c)]. These critical exponents of thermodynamic quantities strongly support the realization of the field-induced transition at  $\mu_0 H_{\rm s}$  as a BEC-QCP of magnons. Although our initial data suggest the possibility of magnon BEC in the 3D limit, further low-temperature experiments in the vicinity of the critical field are required to confirm this behavior more unambiguously. In addition, at  $\mu_0 H_{\rm s}$ , one might expect  $M_{\rm s}-M\propto T^{3/2}$ ; however, due to the limited field range, we are unable to reliably determine the saturation magnetization ( $M_{\rm s}$ ).

In contrast to the BEC observed in 2D systems such as the triangular lattice  $Na_2BaNi(PO_4)_2$  (S = 1) [36] and the honeycomb lattice YbCl<sub>3</sub> ( $J_{\text{eff}} = 1/2$ ) [35] at the saturation field, the present quasi-two-dimensional S = 5/2 system exhibits magnon BEC behavior in the 3D limit, highlighting influence of both interlayer interactions and spin magnitude in governing the nature of quantum phase transitions. Comparatively, the  $S = \frac{5}{2}$  honeycomb-lattice antiferromagnet FeP<sub>3</sub>SiO<sub>11</sub> does not exhibit the BEC scenario, displaying markedly different characteristics from the present compound. This distinction primarily arises from the stronger magnetic anisotropy intrinsic to Fe<sup>3+</sup>-based systems compared with Mn<sup>2+</sup> magnets [45], as reflected in the distinct g values of  $g_1 \approx 2.018$ and  $g_2 \approx 2.001$  in FeP<sub>3</sub>SiO<sub>11</sub> [43]. In addition, although both systems feature comparable nearest-neighbor intraplanar couplings, FeP<sub>3</sub>SiO<sub>11</sub> hosts two additional inequivalent antiferromagnetic interplanar interactions amounting to  $\sim 16.7\%$ and 27.2% of J = 0.863 K [43], whereas KMMO exhibits weak ferromagnetic interplanar coupling  $(J_2 = -0.073 \text{ K})$ alongside with dominant nearest-neighbor antiferromagnetic exchange interactions. Notably, the sizable interplanar interactions in FeP<sub>3</sub>SiO<sub>11</sub>, relative to its intraplanar couplings, give rise to disparate magnetic correlations along the in-plane and out-of-plane directions. These contrasts are further manifested in their transition temperatures and the field-induced evolution of  $T_N$ , leading to distinct field-temperature phase diagrams in the two systems. Our results thus demonstrate

that the combined effects of magnetic anisotropy and interplanar interactions play a decisive role in determining whether a field-induced transition can stabilize BEC criticality, even in systems with the same spin quantum number. Moreover, the occurrence of BEC in magnets with higher spin number underscores the importance of single-site quantum level structure, where multiple spin projection states can enhance magnon interactions. Future high-frequency electron spin resonance experiments are called for to probe magnon bound states near the saturation field.

## IV. CONCLUSION

In summary, we have successfully synthesized single crystals and investigated the thermodynamic properties of a quasi-two-dimensional compound K<sub>4</sub>MnMo<sub>4</sub>O<sub>15</sub>, where  $Mn^{2+}$  ions with S = 5/2 form a honeycomb lattice perpendicular to the c axis, supported by DFT calculations. Our results establish KMMO as a rare example of a quasi-twodimensional honeycomb-lattice antiferromagnet with S =5/2, exhibiting field-tunable quantum critical behavior associated with magnon BEC. A λ-like anomaly in the derivative of magnetic susceptibilities and specific heat confirms the presence of long-range ordered state below  $T_{\rm N} = 2.21$  K, while DFT calculations suggest a dominant intraplanar antiferromagnetic exchange network with weaker interplanar and next-nearest-neighbor intraplanar couplings consistent with the obtained Curie-Weiss temperature. Upon increasing the magnetic field perpendicular to the ab plane, the system exhibits a crossover from Heisenberg to XY anisotropy, followed by a transition to a fully polarized state across the critical field  $\mu_0 H_{\rm s} = 6.4$  T. The observed critical exponent near  $\mu_0 H_s$  highlights the possible realization of a Bose-Einstein condensation quantum critical point in this higher-spin honeycomb lattice. Our study therefore broadens the landscape of BEC associated quantum criticality into a quasi-2D honeycomb lattice with higher spin degrees of freedom. More significantly, our findings provide valuable insight into the conditions under which magnon BEC can emerge in real spin systems with varying interplanar strengths and types of magnetic anisotropy.

#### **ACKNOWLEDGMENTS**

The work at SKKU was supported by the National Research Foundation (NRF) of Korea (Grant No. RS-2023-00209121, 2020R1A5A1016518). S.M.K. and C.-L.H. are supported by the National Science and Technology Council in Taiwan with a Grant No. NSTC 114-2112-M-006-012. R.S. acknowledges the financial support provided by the Ministry of Science and Technology in Taiwan under Projects No. NSTC-113-2124-M-001-003 and No. NSTC-113-2112M001-045-MY3, as well as support from

Academia Sinica for the budget of AS-iMATE11312. fina ncial support from the Center of Atomic Initiative for New Materials (AIMat), National Taiwan University, under Project No. 113L900801.

### DATA AVAILABILITY

The data that support the findings of this article are not publicly available. The data are available from the authors upon reasonable request.

- [1] L. Balents, Spin liquids in frustrated magnets, Nature (London) 464, 199 (2010).
- [2] V. Zapf, M. Jaime, and C. D. Batista, Bose-Einstein condensation in quantum magnets, Rev. Mod. Phys. **86**, 563 (2014).
- [3] J. M. Blatt, K. W. Böer, and W. Brandt, Bose-Einstein condensation of excitons, Phys. Rev. **126**, 1691 (1962).
- [4] D. Wulferding, Y. Choi, S.-H. Do, C. H. Lee, P. Lemmens, C. Faugeras, Y. Gallais, and K.-Y. Choi, Magnon bound states versus anyonic Majorana excitations in the Kitaev honeycomb magnet α-RuCl<sub>3</sub>, Nat. Commun. 11, 1603 (2020).
- [5] J. Kasprzak, M. Richard, S. Kundermann, A. Baas, P. Jeambrun, J. M. J. Keeling, F. M. Marchetti, M. H. Szymańska, R. André, J. L. Staehli, V. Savona, P. B. Littlewood, B. Deveaud, and L. S. Dang, Bose–Einstein condensation of exciton polaritons, Nature (London) 443, 409 (2006).
- [6] E. Fogh, M. Nayak, O. Prokhnenko, M. Bartkowiak, K. Munakata, J.-R. Soh, A. A. Turrini, M. E. Zayed, E. Pomjakushina, H. Kageyama, H. Nojiri, K. Kakurai, B. Normand, F. Mila, and H. M. Rønnow, Field-induced bound-state condensation and spin-nematic phase in SrCu<sub>2</sub>(BO<sub>3</sub>)<sub>2</sub> revealed by neutron scattering up to 25.9 T, Nat. Commun. 15, 442 (2024).
- [7] J. Khatua, B. Sana, A. Zorko, M. Gomilšek, K. Sethupathi, M. S. R. Rao, M. Baenitz, B. Schmidt, and P. Khuntia, Experimental signatures of quantum and topological states in frustrated magnetism, Phys. Rep. 1041, 1 (2023).
- [8] H. Ishikawa, M. Yoshida, K. Nawa, M. Jeong, S. Krämer, M. Horvatić, C. Berthier, M. Takigawa, M. Akaki, A. Miyake, M. Tokunaga, K. Kindo, J. Yamaura, Y. Okamoto, and Z. Hiroi, One-third magnetization plateau with a preceding novel phase in volborthite, Phys. Rev. Lett. 114, 227202 (2015).
- [9] H. Kageyama, K. Yoshimura, R. Stern, N. V. Mushnikov, K. Onizuka, M. Kato, K. Kosuge, C. P. Slichter, T. Goto, and Y. Ueda, Exact dimer ground state and quantized magnetization plateaus in the two-dimensional spin system SrCu<sub>2</sub>(BO<sub>3</sub>)<sub>2</sub>, Phys. Rev. Lett. 82, 3168 (1999).
- [10] T. Giamarchi, C. Rüegg, and O. Tchernyshyov, Bose–Einstein condensation in magnetic insulators, Nat. Phys. 4, 198 (2008).
- [11] T. Nikuni, M. Oshikawa, A. Oosawa, and H. Tanaka, Bose-Einstein condensation of dilute magnons in TlCuCl<sub>3</sub>, Phys. Rev. Lett. 84, 5868 (2000).
- [12] A. F. Andreev and I. A. Grishchuk, Spin nematics, Zh. Eksp. Teor. Fiz. 87, 467 (1984).
- [13] A. Orlova, E. L. Green, J. M. Law, D. I. Gorbunov, G. Chanda, S. Krämer, M. Horvatić, R. K. Kremer, J. Wosnitza, and G. L. J. A. Rikken, Nuclear magnetic resonance signature of the

- spin-nematic phase in  $LiCuVO_4$  at high magnetic fields, Phys. Rev. Lett. 118, 247201 (2017).
- [14] M. Sato, T. Hikihara, and T. Momoi, Spin-nematic and spin-density-wave orders in spatially anisotropic frustrated magnets in a magnetic field, Phys. Rev. Lett. 110, 077206 (2013).
- [15] Y. Kohama, H. Ishikawa, A. Matsuo, K. Kindo, N. Shannon, and Z. Hiroi, Possible observation of quantum spin-nematic phase in a frustrated magnet, Proc. Natl. Acad. Sci. USA 116, 10686 (2019).
- [16] J. Xiang, C. Zhang, Y. Gao, W. Schmidt, K. Schmalzl, C.-W. Wang, B. Li, N. Xi, X.-Y. Liu, H. Jin, G. Li, J. Shen, Z. Chen, Y. Qi, Y. Wan, W. Jin, W. Li, P. Sun, and G. Su, Giant magnetocaloric effect in spin supersolid candidate Na<sub>2</sub>BaCo(PO<sub>4</sub>)<sub>2</sub>, Nature (London) 625, 270 (2024).
- [17] P. Sengupta and C. D. Batista, Field-induced supersolid phase in spin-one Heisenberg models, Phys. Rev. Lett. 98, 227201 (2007).
- [18] Ch. Rüegg, N. Cavadini, A. Furrer, H.-U. Güdel, K. Krämer, H. Mutka, A. Wildes, K. Habicht, and P. Vorderwisch, Bose– Einstein condensation of the triplet states in the magnetic insulator TlCuCl<sub>3</sub>, Nature (London) 423, 62 (2003).
- [19] V. S. Zapf, D. Zocco, B. R. Hansen, M. Jaime, N. Harrison, C. D. Batista, M. Kenzelmann, C. Niedermayer, A. Lacerda, and A. Paduan-Filho, Bose-Einstein condensation of *S* = 1 nickel spin degrees of freedom in NiCl<sub>2</sub>-4SC(NH<sub>2</sub>)<sub>2</sub>, Phys. Rev. Lett. 96, 077204 (2006).
- [20] M. Jaime, V. F. Correa, N. Harrison, C. D. Batista, N. Kawashima, Y. Kazuma, G. A. Jorge, R. Stern, I. Heinmaa, S. A. Zvyagin, Y. Sasago, and K. Uchinokura, Magnetic-field-induced condensation of triplons in Han purple pigment BaCuSi<sub>2</sub>O<sub>6</sub>, Phys. Rev. Lett. 93, 087203 (2004).
- [21] M. Greiner, O. Mandel, T. Esslinger, T. W. Hänsch, and I. Bloch, Quantum phase transition from a superfluid to a Mott insulator in a gas of ultracold atoms, Nature (London) 415, 39 (2002).
- [22] B. S. Conner, H. D. Zhou, Y. J. Jo, L. Balicas, C. R. Wiebe, J. P. Carlo, Y. J. Uemura, A. A. Aczel, T. J. Williams, and G. M. Luke, Possible Bose-Einstein condensate of magnons in single-crystalline Pb<sub>2</sub>V<sub>3</sub>O<sub>9</sub>, Phys. Rev. B 81, 132401 (2010).
- [23] S. E. Sebastian, N. Harrison, C. D. Batista, L. Balicas, M. Jaime, P. A. Sharma, N. Kawashima, and I. R. Fisher, Dimensional reduction at a quantum critical point, Nature (London) 441, 617 (2006).
- [24] A. A. Aczel, Y. Kohama, M. Jaime, K. Ninios, H. B. Chan, L. Balicas, H. A. Dabkowska, and G. M. Luke, Bose-Einstein

- condensation of triplons in Ba<sub>3</sub>Cr<sub>2</sub>O<sub>8</sub>, Phys. Rev. B **79**, 100409 (2009).
- [25] A. Vasiliev, O. Volkova, E. Zvereva, and M. Markina, Milestones of low-D quantum magnetism, npj Quantum Mater. 3, 18 (2018).
- [26] T. Radu, Y. Tokiwa, R. Coldea, P. Gegenwart, Z. Tylczynski, and F. Steglich, Field induced magnetic phase transition as a magnon Bose Einstein condensation, Sci. Technol. Adv. Mater. 8, 406 (2007).
- [27] T. Radu, H. Wilhelm, V. Yushankhai, D. Kovrizhin, R. Coldea, Z. Tylczynski, T. Lühmann, and F. Steglich, Bose-Einstein condensation of magnons in Cs<sub>2</sub>CuCl<sub>4</sub>, Phys. Rev. Lett. 95, 127202 (2005).
- [28] P. J. Baker, T. Lancaster, S. J. Blundell, M. L. Brooks, W. Hayes, D. Prabhakaran, and F. L. Pratt, Thermodynamic and magnetic properties of the layered triangular magnet NaNiO<sub>2</sub>, Phys. Rev. B 72, 104414 (2005).
- [29] L.J. de Jongh and H.J.M. de Groot, Phase diagrams of weakly anisotropic Heisenberg antiferromagnets: II. Quasi 2dimensional systems, Solid State Commun. 53, 737 (1985).
- [30] T. Matsubara and H. Matsuda, A lattice model of liquid helium, I, Prog. Theor. Phys. **16**, 569 (1956).
- [31] E. G. Batyev and L. S. Braginskii, Antiferrornagnet in a strong magnetic field: Analogy with Bose gas, Sov. Phys. JETP 60, 781 (1984).
- [32] N. D. Mermin and H. Wagner, Absence of ferromagnetism or antiferromagnetism in one- or two-dimensional isotropic Heisenberg models, Phys. Rev. Lett. 17, 1133 (1966).
- [33] V. L. Berezinskii, Destruction of long-range order in onedimensional and two-dimensional systems possessing a continuous symmetry group. II. Quantum systems, Sov. Phys. JETP 34, 610 (1972).
- [34] J. M. Kosterlitz and D. J. Thouless, Long range order and metastability in two dimensional solids and superfluids. (application of dislocation theory), J. Phys. C: Solid State Phys. 5, L124 (1972).
- [35] Y. Matsumoto, S. Schnierer, J. A. N. Bruin, J. Nuss, P. Reiss, G. Jackeli, K. Kitagawa, and H. Takagi, A quantum critical Bose gas of magnons in the quasi-two-dimensional antiferromagnet YbCl<sub>3</sub> under magnetic fields, Nat. Phys. 20, 1131 (2024).

- [36] J. Sheng, J.-W. Mei, L. Wang, X. Xu, W. Jiang, L. Xu, H. Ge, N. Zhao, T. Li, A. Candini, B. Xi, J. Zhao, Y. Fu, J. Yang, Y. Zhang, G. Biasiol, S. Wang, J. Zhu, P. Miao, X. Tong *et al.*, Bose–Einstein condensation of a two-magnon bound state in a spin-1 triangular lattice, Nat. Mater. 24, 544 (2025).
- [37] M. Prüfer, D. Spitz, S. Lannig, H. Strobel, J. Berges, and M. K. Oberthaler, Condensation and thermalization of an easy-plane ferromagnet in a spinor Bose gas, Nat. Phys. 18, 1459 (2022).
- [38] Y. Watanabe, A. Miyake, M. Gen, Y. Mizukami, K. Hashimoto, T. Shibauchi, A. Ikeda, M. Tokunaga, T. Kurumaji, Y. Tokunaga, and T.-hisa Arima, Double dome structure of the Bose–Einstein condensation in diluted S = 3/2 quantum magnets, Nat. Commun. 14, 1260 (2023).
- [39] T. Ozaki, Variationally optimized atomic orbitals for large-scale electronic structures, Phys. Rev. B 67, 155108 (2003).
- [40] H. Yoon, T. J. Kim, J.-H. Sim, and M. J. Han, Jx: An opensource software for calculating magnetic interactions based on magnetic force theory, Comput. Phys. Commun. 247, 106927 (2020).
- [41] S. F. Solodovnikov, E. S. Zolotova, and Z. A. Solodovnikova, Crystal structure of  $K_2MnMo_4O_{15}$  A parent compound of a new isostructural series of complex oxides  $K_2Mn^{2+}Mo_4O_{15}$  ( $M^{2+} = Mn, Mg, Co, Cd$ ), J. Struct. Chem. **38**, 83 (1997).
- [42] J. Khatua, T. Arh, S. B. Mishra, H. Luetkens, A. Zorko, B. Sana, M. S. R. Rao, B. R. K. Nanda, and P. Khuntia, Development of short and long-range magnetic order in the double perovskite based frustrated triangular lattice antiferromagnet Ba<sub>2</sub>MnTeO<sub>6</sub>, Sci. Rep. 11, 6959 (2021).
- [43] J. Khatua, M. Gomilšek, K.-Y. Choi, and P. Khuntia, Magnetism and field-induced effects in the  $S = \frac{5}{2}$  honeycomb lattice antiferromagnet FeP<sub>3</sub>SiO<sub>11</sub>, Phys. Rev. B **110**, 184402 (2024).
- [44] A. I. Liechtenstein, M. I. Katsnelson, V. P. Antropov, and V. A. Gubanov, Local spin density functional approach to the theory of exchange interactions in ferromagnetic metals and alloys, J. Magn. Magn. Mater. 67, 65 (1987).
- [45] Z. Ur Rehman, Z. Muhammad, O. Adetunji Moses, W. Zhu, C. Wu, Q. He, M. Habib, and L. Song, Magnetic isotropy/anisotropy in layered metal phosphorous trichalcogenide MPS3 (M = Mn, Fe) single crystals, Micromachines 9, 292 (2018).